OPTICA

Single-pulse, reference-free, spatiospectral measurement of ultrashort pulse-beams

David Goldberger,[1,*] Jonathan Barolak,[1] Charles S. Bevis,[2] Bojana Ivanic,[1] David Schmidt,[1] Yuhao Lei,[3] Peter Kazansky,[3] Giulia F. Mancini,[2] Charles G. Durfee,[1] and Daniel E. Adams[1]

[1]Department of Physics, Colorado School of Mines, 1523 Illinois Street, Golden, Colorado 80401, USA
[2]Laboratory for Ultrafast X-ray and Electron Microscopy, Department of Physics, University of Pavia, Via Agostino Bassi 6, 27100 Pavia PV, Italy
[3]Optoelectrics research center, University of Southampton, SO17 1BJ, Southampton, UK
*Corresponding author: dgoldberger@mines.edu

Received 28 April 2022; revised 12 July 2022; accepted 13 July 2022; published 3 August 2022

High-intensity pulse-beams are ubiquitous in scientific investigations and industrial applications ranging from the generation of secondary radiation sources (e.g., high harmonic generation, electrons) to material processing (e.g., micromachining, laser-eye surgery). Crucially, pulse-beams can only be controlled to the degree to which they are characterized, necessitating sophisticated measurement techniques. We present a reference-free, full-field, single-shot spatiospectral measurement technique called broadband single-shot ptychography (BBSSP). BBSSP provides the complex wavefront for each spectral and polarization component in an ultrafast pulse-beam and should be applicable across the electromagnetic spectrum. BBSSP will dramatically improve the application and mitigation of spatiospectral pulse-beam structure.

https://doi.org/10.1364/OPTICA.462586

1. INTRODUCTION

Reaching the highest possible laser intensities requires tight focusing in both space and time. Spatiotemporally focused, ultrafast laser pulse-beams deliver extreme intensities that are used for high harmonic generation [1–4], electron acceleration (e.g., wakefield, pondermotive) [5–7], filamentation [8–10], micromachining [11,12], and other practical and scientific applications. Higher pulse-beam intensities would enable investigation of extreme physical phenomena, e.g., the Schwinger limit [13]. For pulse-beams of fixed energy, maximizing focal intensity requires a carefully tailored pulse-beam structure. Aside from maximizing intensity, pulse-beam structures can also be engineered for various applications (simultaneous spatial and temporal focusing (SSTF), stimulated emission depletion microscopy (STED), and micromachining) [11,12,14–18]. Crucially, these can only be controlled to the degree to which they are characterized, necessitating sophisticated pulse-beam measurement techniques.

Measuring ultrafast laser pulse-beams has been a challenge since their discovery [19,20]. Conventional pulse measurement techniques, like frequency resolved optical gating measure temporal profiles at one position in space, are averaged over the beam profile, or they assume a uniform temporal profile across the beam's spatial profile [21–23]. Similarly, conventional beam or wavefront measurement techniques like Shack–Hartmann wavefront sensors measure temporally averaged spatial profiles and provide no information about the temporal profile [24]. The ideal pulse-beam measurement technique would provide the spatially resolved temporal profile for each polarization component in the pulse-beam electric field, i.e., spatiotemporal characterization of $\boldsymbol{E}(x, y, z, t) \equiv \boldsymbol{E}(\boldsymbol{r}, t)$ [25–27] (bold symbols represent vectors). For one field component, the spatiotemporal profiles of ultrashort pulse-beams are too short to be measured directly, but they can be calculated as $E(\boldsymbol{r}, t) = \mathscr{F}^{-1}\{\tilde{E}(\boldsymbol{r}, \omega)\}$, where $\mathscr{F}$ is the temporal Fourier transform and $\tilde{E}(\boldsymbol{r}, \omega)$ is the complex spatiospectral profile of the ultrashort pulse-beam. As such, spatiospectral characterization of ultrashort pulse-beams is critical. Due to couplings, the complex profile of an ultrafast pulse-beam is not necessarily separable, e.g., $E(\boldsymbol{r}, t) \neq E(\boldsymbol{r})\mathscr{F}^{-1}\{\tilde{E}(\omega)\}$, so independent spectral/temporal and spatial measurement is insufficient [28,29]. Many techniques have been developed for spatiospectral characterization, but they require scanning, a reference beam, or only characterize a single spatial dimensions of the pulse-beam as detailed in Supplement 1, Section 1 [25,26,30–39]. One such spatiospectral characterization technique is broadband ptychography, which we recently demonstrated [40].

Ptychography was developed as a phase-sensitive microscopic imaging technique. In ptychography, diffraction patterns associated with overlapping regions of a sample, called an object, are recorded by translating a spatially constrained illumination, called a probe, transverse to the object [41–44]. Originally, ptychographic phase retrieval algorithms relied on known probe profiles that could be used as constraints, but [45,46] showed that there was enough redundancy in a ptychographic data set to allow for simultaneous reconstruction of the object and probe,

and that algorithmic reconstruction of the illumination improved reconstruction fidelity. The ability to reconstruct the complex, phase-and-amplitude, spatial profile, or wavefront, of the illumination is key for pulse-beam metrology by ptychography. Here, instead of using ptychography to image a microscopic object, we use ptychography to "image" light itself. It is important to note that ptychography reconstructs the spatial profile of the pulse-beam as it appeared *before* interacting with the object.

In broadband ptychography, the goal is to reconstruct the quasi-monochromatic, complex, beam profile of each spectral channel, which represents the sum of the illumination over the sub-bandwidth of the binned spectrum [47]. In other words, each spectral channel in the reconstruction yields a beamlet with electric field: $\tilde{E}(x, y, \omega_j) = \frac{1}{\epsilon}\int_{\omega_j-\epsilon/2}^{\omega_j+\epsilon/2} \tilde{E}(x, y, \omega')\mathrm{d}\omega'$. By increasing the number of reconstructed wavelength channels (decreasing the sub-bandwidth ϵ), this approximation becomes more accurate [40]. Since the complex field is reconstructed, this result can be propagated axially to give $\tilde{E}(\boldsymbol{r}, \omega_j)$. Thus, broadband ptychography enables characterization of focused pulse-beams by making measurements away from focus. Broadband ptychography does not provide the spectral phase, which precludes full spatiotemporal characterization, but it is still an attractive technique for pulse-beam metrology because it measures the full two-dimensional probe field at the object plane, it does not require a reference beam, data can be collected in a single shot, and it allows for various forms of multiplexing [48–50]. Any measured diffraction pattern that can be written as the sum of mutually incoherent diffraction patterns can be demultiplexed, regardless of the physical source of the incoherence [51]. Physical sources of mutual incoherence include: multiple wavelengths, orthogonal polarization states, and temporal separation. Critically, multiple physical sources of incoherence can be demultiplexed simultaneously, which is crucial for full single-shot pulse-beam characterization. [50,52–56].

2. METHODS

In this work, we present the first single-shot, reference-free, full-field, simultaneous phase-and-amplitude reconstruction of each frequency and polarization state in an incident pulse-beam. Our novel technique is called broadband single-shot ptychography (BBSSP), and to emphasize its utility we use it to characterize a single pulse. Many single-shot ptychography (SSP) systems use diffractive optical elements (DOEs) like pinhole or lenslet arrays to break up incident illumination spatially, which precludes beam metrology [57]. Our novel BBSSP system, shown in Fig. 1(a), uses a two-dimensional diffractive beam splitter DOE, or grating, which is similar to the initial demonstration of SSP [58]. For a single wavelength, the grating DOE used in this work produces copies of the incident illumination with equal power in each order that propagate in directions determined by the grating equation. For multiple wavelengths within a single diffracted order, the dispersive nature of the grating must be taken into account. The grating dispersion can be seen in Fig. 1(b). It necessitates changes to the ptychographic phase retrieval algorithm, which are presented in Supplement 1, Section 3. Critically, we find that after appropriate algorithmic modification the grating dispersion improves spectral discrimination.

A. BBSSP System

The full experimental system is described in Supplement 1, Section 2. The BBSSP system shown in Fig. 1 consists of four optical components. The two-dimensional diffractive beam splitter, or grating, produces roughly equal intensity copies of the input illumination in each of the diffracted orders, $M_x, M_y = \{0, \pm1, \pm2, \pm3\}$, except for the 0, 0 order. This gives 48 copies of the incident illumination, called beamlets. For pulse-beam characterization, the goal is to reconstruct the spectrally resolved wavefronts, so we have freedom to choose a convenient object. We use a binary, amplitude-only object, which gives two advantages: first, achromatic objects are amenable to object averaging [40]; second, comparison of the reconstructed and known spatial profiles of the object provides a fidelity check that gives confidence in the accuracy of the reconstruction results. If the object is characterized well enough, for instance in calibration, the object's spatial profile can be used as a constraint to improve the quality and speed of reconstruction. All the experiments presented here use a thin, amplitude-only, copper SEM finder grid. The object is placed a short distance δ downstream of the grating. Regardless of δ, a Fourier-transform lens is placed one focal length away from the grating. A detector is placed one focal length downstream of the Fourier-transform lens.

B. Data Collection

We followed similar data collection procedures for all the experiments we performed. Every data set we collect consists of at least one spectrometer measurement and four images: a single exposure and a high dynamic range (HDR) image of the beam, and a single exposure and an HDR image of the diffraction data. The beam images are taken without the object in the system, and they are used for modulus enforcement on the probe (MEP) [59]. Even though four images (10 exposures) are always collected, they are not always used in reconstruction. The single-pulse-beam reconstruction (Section 3.A), for instance, only uses one single exposure image of the diffraction data. The HDR images are collected by stitching together four exposures of 1, 16, 256, and 4096 ms. The use of HDR gives a better sense for the capabilities of BBSSP uncoupled

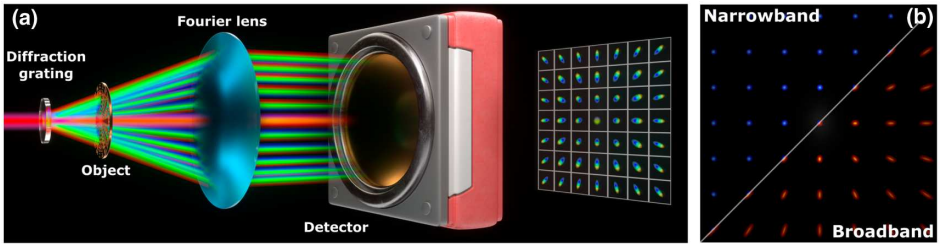

Fig. 1. BBSSP system and beam data comparison. (a) Broadband single-shot ptychography (BBSSP) system and false color beam image array. (b) Example of beam data, collected without the object in the system, for narrowband (top left) and broadband (bottom right) illumination.

from the limited dynamic range of our specific detector, which could be improved by using a detector with higher dynamic range. For each data set, we measured the spatially averaged spectrum of the pulse-beam at the focal plane between the two imaging lenses on a fiber coupled spectrometer. Comparison of the measured and reconstructed spatially averaged spectra serves as a fidelity check for reconstruction accuracy.

C. Algorithm

All the reconstructions presented here used the same ptychographic reconstruction algorithm: a modified version of the "PIM-RAAR" algorithm developed for broadband ptychography. PIM-RAAR is described in detail in the supplementary information of Ref. [40]. PIM-RAAR is particularly well suited to broadband ptychography, but any ptychographic phase retrieval algorithm can be used with BBSSP once it is modified appropriately. Specifically, the algorithms must be adapted to account for the grating dispersion, which necessitates two changes. The first algorithmic modification is that the positions of the beamlets on the object become wavelength dependent. The second algorithmic modification accounts for wavelength-dependent propagation of the beamlets between the object and the detector. Accurate application of these modifications requires the positions of a known wavelength on the detector (which are geometrically related to the positions at the object). If the system is perfectly aligned, the positions can be calculated from known grating parameters, but empirically we found that calibration with a narrowband source provides better results. The algorithmic modifications are described in detail in Supplement 1, Section 3. With appropriate algorithmic modifications, any ptychographic phase retrieval algorithm could be used with the BBSSP system.

Two particularly useful capabilities of the PIM-RAAR algorithm for beam metrology with BBSSP are object averaging and MEP [40,47,59]. Averaging reconstructed objects from different spectral channels constrains the PIM-RAAR algorithm so that it must reconstruct an achromatic object, which improves results. We use an achromatic object described in Section 2.A, and we always use object averaging for the broadband reconstructions. MEP also provides a strong constraint that improves reconstructions, but it requires collection of a beam image without the object in the BBSSP system. For stable pulse trains, the beam image can be thought of as an additional calibration step that can be performed before single-shot data acquisition. However, if pulse-to-pulse fluctuations are significant, the pulse measured in the beam image may be substantially different from the pulse measured in the diffraction data, and the MEP constraint may not be appropriate. To demonstrate general single-pulse-beam measurement, the single-pulse results shown in Section 3.A were reconstructed without the use of the MEP constraint. All the other results presented used the MEP constraint. The beam image required for the MEP constraint could be collected with the diffraction data in a single shot through modifications or additions to the BBSSP system. For instance, an object could be designed with a gap in it to ensure that one or more beamlet passes through free space. Then that beamlet would provide the required beam image. Alternatively, an amplitude beam splitter and an additional synchronized detector could be used to collect the beam image.

3. RESULTS

We performed a series of experiments to demonstrate single-shot, reference-free, full-field, spatiospectral characterization of ultrafast pulse-beams with BBSSP, including characterization of a single-pulse-beam. First, we present reconstructions of the complex, spatiospectral profile of a single roughly Gaussian pulse-beam from a Ti:sapphire amplifier and of Gaussian pulse-beams from a mode-locked Ti:Sapphire oscillator. Next, we demonstrate spatiospectral characterization of a vortex pulse-beam carrying orbital angular momentum (OAM). Then, we validate the technique by presenting reconstructions of a spatiospectrally structured pulse-beam. Finally, we present spatiospectral reconstructions of orthogonal polarization states within a vector pulse-beam [60] to display the polarization sensitivity of BBSSP, which is unique among single-shot spatiospectral characterization techniques. Reconstruction details for each experiment are in Supplement 1, Section 10. Our comprehensive demonstration of the applicability of our novel method to a host of key cases makes our approach relevant and applicable to virtually any ultrafast installation, from compact tabletop to large-scale facilities like free electron lasers (FELs).

A. Characterization of Single-Pulse and Multipulse Gaussian Beams

The primary advantage of the single-shot nature of BBSSP is the ability to measure a single-pulse-beam. When pulse-to-pulse fluctuations are significant, accurate measurement requires characterization of individual pulse-beams. To validate single-pulse-beam characterization with BBSSP we used a Ti:sapphire amplifier system. The amplifier's repetition rate is 1 kHz, so by setting the exposure time of our detector to 0.9 ms we ensure that only illumination from a single-pulse-beam is measured.

Pulse-beams with Gaussian spatial and temporal profiles provide a convenient mathematical framework for matching simulation to experiments and are ubiquitous. Ultrafast pulse-beams are often roughly Gaussian in space and time/spectrum with alterations caused by aberrations and/or chromaticity from imperfect or imperfectly aligned optics. Since Gaussian pulse-beams are convenient and common, they are a good starting point for validation of spatiospectral characterization by BBSSP. Figure 2 demonstrates spatiospectral characterization of a nearly Gaussian single-pulse-beam from the Ti:sapphire amplifier. We used an interference filter to reduce the bandwidth of the amplified illumination for calibration purposes only. Reconstructions of the narrowband amplified beam are shown in Figs. 2(a) and 2(b). Comparison of the reconstructed object transmission profile, Fig. 2(a), with the ground truth, shown in the inset, serves as a fidelity check to ensure accurate pulse-beam reconstruction. After collecting the calibration data set, the interference filter was removed and we collected the single-pulse-beam data set. Reconstruction of the single-pulse-beam was performed with eight spectral channels of 10 nm subbandwidth covering a total bandwidth of 760 to 830 nm. Figure 2(c) shows the reconstructed object transmission profile, and row (i) shows selected spectrally resolved probe fields. Figure 2(d) shows the measured spatially averaged spectra from the amplifier and from the reconstruction of the single-pulse-beam. Comparison of the measured and reconstructed spectra serves as another fidelity check for reconstruction accuracy. As expected, the reconstruction indicates that all the spectral components have nearly ideal Gaussian spatial profiles. **Note that while only the**

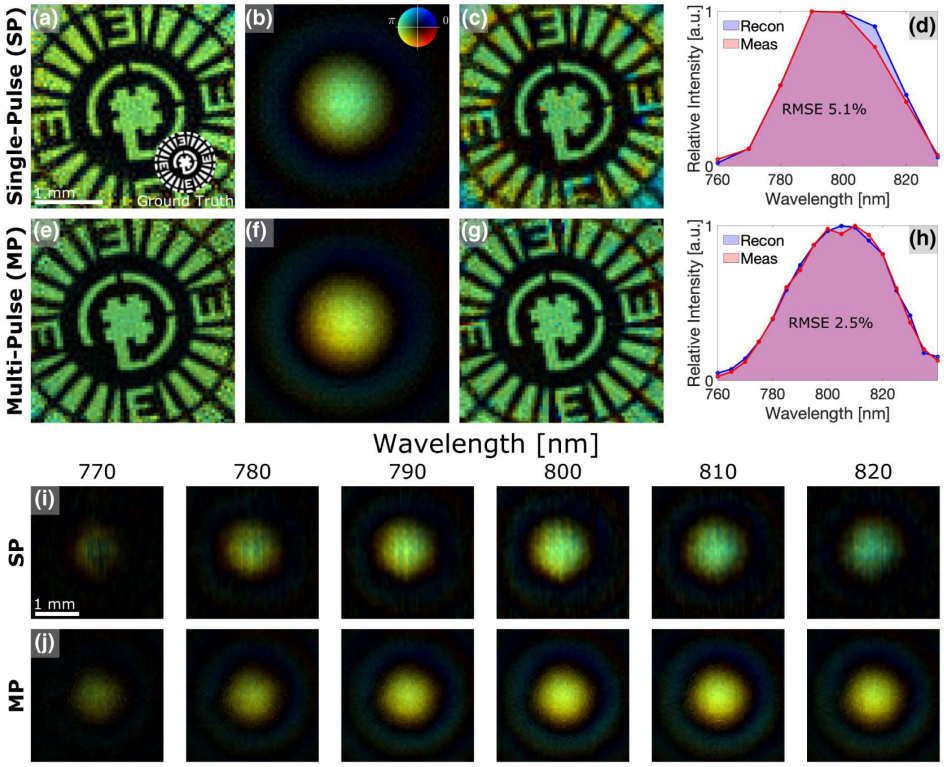

Fig. 2. Single-pulse and multipulse Gaussian reconstructions. (a) Reconstructed object transmission profile (ground truth shown as inset); (b) reconstructed probe field, from the single channel reconstruction of the narrowband amplified beam used for calibration. The scale bar in (a) is common to (a)–(c) and (e)–(g). (c) Reconstructed object transmission profile for the broadband amplified single-pulse-beam. (d) Measured spatially averaged spectra from the amplifier and from the reconstruction of the single-pulse-beam. The root mean square error (RMSE) between the reconstructed and measured spatially averaged spectra is 5.1%. (e) Reconstructed object transmission profile; (f) reconstructed probe field, from the single channel reconstruction of the narrowband Gaussian oscillator beam used for calibration. (g) Reconstructed object transmission profile for the broadband oscillator pulse-beam. (h) Measured and reconstructed spatially averaged spectra for the broadband oscillator pulse-beam. The RMSE between the reconstructed and measured spatially averaged spectra is 2.5%. Rows (i)–(j): Selected spectrally resolved probe channels from a single amplified pulse-beam and from the oscillator pulse-beam, respectively. The scale bar in (i) is common for both rows. All the reconstructed channels are shown in Supplement 1, Fig. S6. In all cases the complex field is shown with brightness representing amplitude and color representing phase.

spatially averaged spectrum is shown in the figure, our reconstruction yields the spectrum at each spatial position in the reconstruction grid. In other words, here we retrieve the spatially resolved spectrum of the pulse-beam with spatial resolution of about 45 μm, over a field of view of about 14.5 mm (Supplement 1, Section 2).

Besides single-pulse-beam characterization, the single-shot nature of BBSSP is beneficial because it reduces data collection time and removes scan position uncertainty. Figures 2(e)–2(h) and row (j) demonstrate spatiospectral characterization of nearly Gaussian pulse-beams from a modelocked Ti:sapphire oscillator. Reconstructions of the narrowband Gaussian oscillator beam, used for calibration, are shown in (e) and (f). The broadband Gaussian oscillator beam was reconstructed with 17 spectral channels of 5 nm subbandwidth covering a total bandwidth of 760 to 840 nm. Figure 2(g) shows the reconstructed object, and (h) shows the measured and reconstructed spatially averaged spectra. Figure 2(j) shows selected reconstructed spectrally resolved probe fields. These results confirm that BBSSP provides accurate spatiospectral characterization of Gaussian pulse-beams, including single-pulse-beams. Supplement 1, Section 7 and Fig. S5 present further discussion about the difference between single-pulse and multipulse characterization with BBSSP.

B. Characterization of Pulse-Beam Carrying OAM

To demonstrate the ability of BBSSP to reconstruct pulse-beams with complicated spatial structures, we characterized a vortex pulse-beam with OAM. Besides their application in visible optics, soft to hard x-ray OAM beams generated in synchrotrons and FELs have proven effective—for example, for the detection of chirality in matter through helical dichroism [61,62]. To generate a spatially structured pulse-beam, we placed an $m = 1$ spiral glass vortex plate in the image plane of the object. The plate is designed to impart a $0 - 2\pi m$ azimuthal phase wrap for 800 nm light. We performed the experiment with narrowband illumination for calibration and with the full bandwidth from the oscillator. Figures 3(a) and 3(b) show the results from the reconstruction of the narrowband vortex beam. The reconstructed object compares well with the ground truth shown in the inset. The slight linear phase along the horizontal axis is likely due to an object tilt of about 6 mrad. The reconstructed probe shows a phase profile that wraps azimuthally from 0 to 2π, i.e., it has an OAM charge of 1. The broadband vortex beam was reconstructed with 17 spectral channels of 5 nm subbandwidth covering a total bandwidth of 760 to 840 nm. Figure 3(c) shows the reconstructed object, and (d) shows the reconstructed and measured spatially averaged spectra for the broadband reconstruction. Row (e) shows selected spectrally resolved probe fields. BBSSP is ideal for characterizing OAM

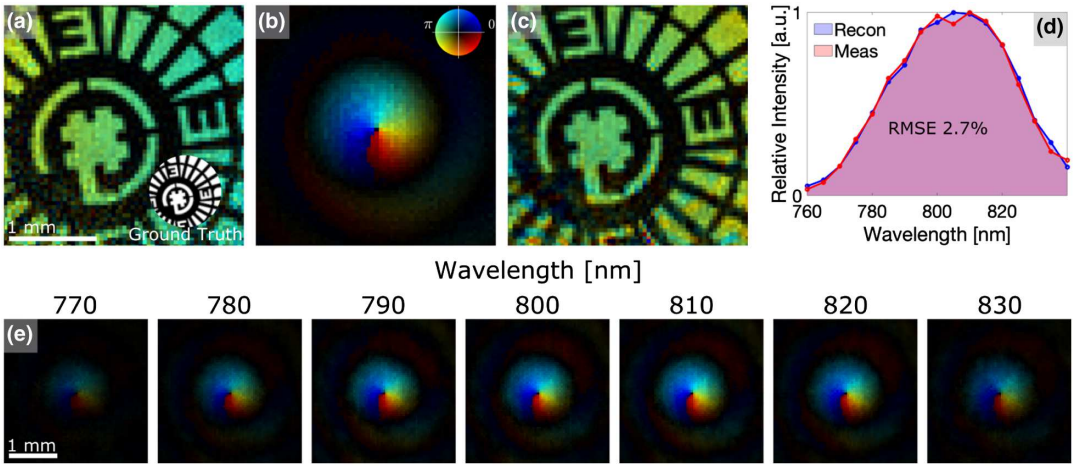

Fig. 3. Vortex pulse-beam reconstruction. (a) Reconstructed object transmission profile, (ground truth shown as inset); (b) reconstructed probe field, from the single channel reconstruction of the narrowband vortex beam used for calibration. The scale bar in (a) is common to (a)–(c). (c) Reconstructed object transmission profile for the broadband vortex pulse-beam; (d) reconstructed and measured spatially averaged spectra for the vortex pulse-beam. RMSE between the reconstructed and measured spatially averaged spectra is 2.7%. Row (e): Selected spectrally resolved probe fields (all channels are shown in Supplement 1, Fig. S6). The scale bar in (e) is common to the row. In all cases the complex field is shown with brightness representing amplitude and color representing phase.

pulse-beams. Its high spatial resolution and phase sensitivity enable precise measurement of OAM states in a single shot. As explained in [63], a spectrally dependant OAM state is not expected, despite the fact that a physical spiral glass structure was used to impart the vortex phase. This is confirmed in our measurement, as each of the spectrally resolved probe fields show OAM charge of 1.

C. Characterization of a Spatiospectrally Structured Pulse-Beam

A spatiospectrally structured pulse-beam exhibits different spectral profiles across its spatial profile. For our experiment, we generated a spatiospectrally structured pulse-beam by placing a neodymium-doped vanadate crystal (Nd:YVO4) in the image plane of the object, oriented such that roughly a quarter of the otherwise Gaussian pulse-beam passed through the crystal. Absorption in the crystal alters the spectrum of the part of the pulse-beam that passes through it, creating a spatiospectrally structured pulse-beam. We performed the experiment with narrowband illumination for calibration and with the full bandwidth of the oscillator pulse-beam. For both experiments, we performed reconstructions with either one or two mutually incoherent channels (MIC) allowed for each spectral channel. In all cases, the reconstructions provided reasonable results, but we found that allowing for two MIC within each spectral channel significantly improved reconstructions. Figure 4 shows the results from the two-channel reconstructions. For simplicity, only the summed intensity of the MICs are shown for selected spectral channels. The individual MICs are shown in Supplement 1, Fig. S6. For the narrowband beam and for each spectral channel in the broadband pulse-beam, the algorithm divides the illumination into two MICs in the same way. In one channel, the portion of the beam that passes through the crystal is dimmer than the other portion, and there is no phase difference between them. In the other channel, the portion of the beam that passes through the crystal has roughly the same intensity as the other portion, and the two portions are about π out of phase. The most likely source of the observed incoherence is the delay from the vanadate crystal, which slows the light that passes through it such that it no longer temporally overlaps with the light that does not. The vanadate crystal is 2 mm thick, and its index of refraction is about 1.97 at 800 nm, so light that passes through the crystal is delayed by about 6.5 picoseconds relative to light that does not, neglecting edge diffraction. Since the two portions of the illumination are temporally separated, they are mutually incoherent, and the algorithm finds a better solution by allowing for two MICs, referred to as temporal channels, for each spectral channel in the illumination. Likely the reason that we observe energy both inside and outside the crystal region in each temporal channel is due to edge diffraction from the relatively thick crystal. This result emphasizes the utility of pulse-beam metrology by ptychography as the method can diagnose sources of mutual incoherence in the pulse-beam.

Accurately reconstructing the spatial dependence of the spectrum is critical to demonstrating characterization of a spatiospectrally structured pulse-beam. In addition to recording the spatially averaged spectrum of the pulse-beam, we made two more spectrometer measurements for the spatiospectrally structured pulse-beam: we measured the spectrum when the full oscillator pulse-beam passed through the crystal [Fig. 4(f)] and without the crystal in the system [Fig. 4(e)]. Figures 4(a) and 4(c) show the results from the reconstruction of the narrowband beam used for calibration. The broadband spatiospectrally structured pulse-beam was reconstructed with 17 spectral channels of 5 nm subbandwidth covering a total bandwidth of 760 to 840 nm and two temporal channels for each spectral channel. Thus, there are a total of 34 MICs in the reconstruction. Figure 4(b) shows the summed intensity of all 34 probe channels reconstructed from the broadband pulse-beam. The summed intensity image compares well with a CCD image of the same pulse-beam, which is shown as an inset in (c). The second row shows (d) the measured spatially averaged spectrum with the crystal a quarter of the way into the beam, (e) with no crystal in the system, and (f) with the full pulse-beam passing through the crystal. In (d) the spatially averaged reconstructed spectrum of the full beam is shown for comparison, but in (e) the reconstructed spectrum is only spatially averaged over a subset of

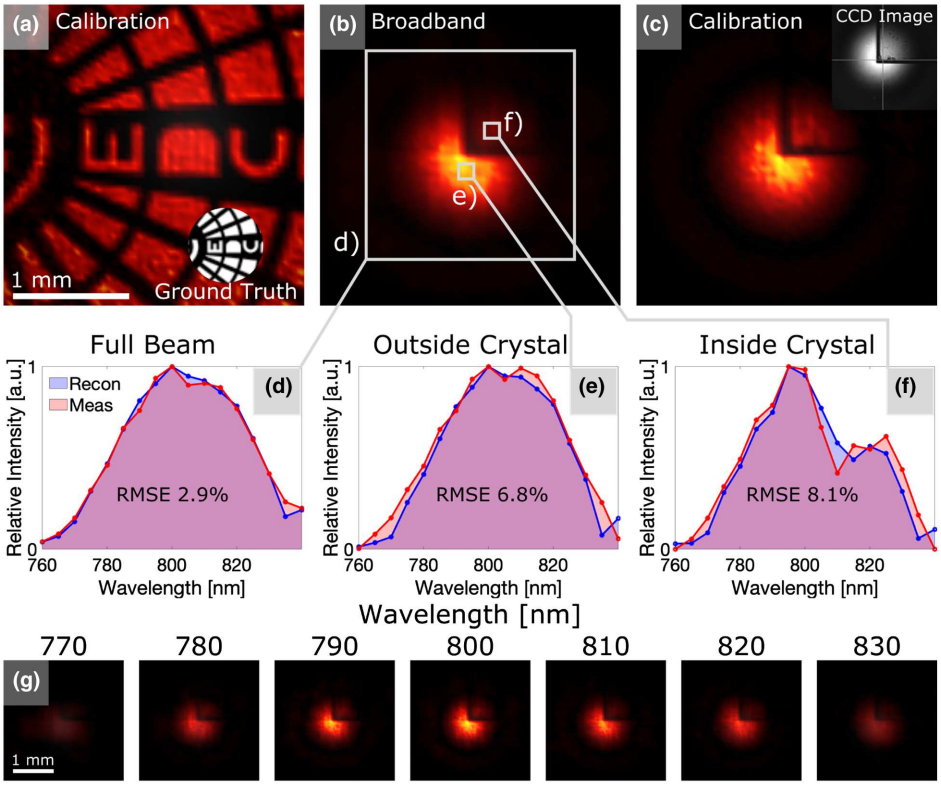

Fig. 4. (a) Reconstructed object transmission; (c) reconstructed summed probe intensity from two-temporal-channel (single-spectral-channel) reconstruction of the narrowband pulse-beam used for calibration. The scale bar in (a) is common for (a)–(c). (b) Summed intensity of all reconstructed probe channels for the spatiospectrally structured pulse-beam; the inset in (c) shows a CCD image of the same beam for comparison. (d) Reconstructed and measured spatially averaged spectra of the full beam with the crystal a quarter of the way into the beam. (e) Measured spatially averaged spectrum without the crystal and reconstructed spectrum measured outside the crystal—lower square in (b). (f) Measured spatially averaged spectrum through crystal and reconstructed spectrum measured inside the crystal—upper right white square in (b). The RMSE for each of the spectral comparisons is shown in the corresponding panel. Row (g) shows selected spectrally resolved summed probe intensities. The scale bar in (g) is common to the row. The individual MICs and the spectrally resolved summed intensities are shown in Supplement 1, Fig. S6.

pixels outside of the crystal, [lower square in (b)], while in (f) the reconstructed spectrum is only spatially averaged over a subset of pixels inside the crystal [upper right square in (b)]. Figure 4(g) shows selected spectrally resolved probe intensities, which are calculated as the summed intensity of the two temporal channels for each spectral channel. The agreement between the reconstructed and measured spatially averaged spectra inside and outside the crystal indicates that BBSSP accurately reconstructions the spatial dependence of pulse-beam spectra.

D. Polarization Sensitivity

The experiments presented thus far show that BBSSP provides full-field, reference-free, single-shot spatiospectral characterization of ultrafast pulse-beams. Here we highlight an important unique capability of BBSSP that makes it attractive for pulse-beam metrology. Since two orthogonally polarized pulse-beams cannot interfere with one another, a pulse-beam that consists of different polarizations can be decomposed into two MICs with each channel representing one of the orthogonal polarizations in the pulse-beam [50,52,55]. BBSSP supports simultaneous demultiplexing of multiple sources of incoherence if all reconstructed probe channels are mutually incoherent. Thus, we can use BBSSP to image the spatiospectral profile of orthogonal polarizations in a pulse-beam. To our knowledge, no other spatiospectral characterization technique can simultaneously characterize orthogonal polarization states in a pulse-beam.

To generate a polarization structured (vector) pulse-beam, we placed a custom s-wave plate, designed and fabricated by the Kazansky Group at the University of Southampton, at the image plane of the object. Details of the *s*-wave plate fabrication are in Supplement 1, Section 6. In addition to the normal narrowband calibration data, we took two data sets with a linear polarizer placed after the first imaging lens oriented to transmitted horizontal and then vertical polarization. The two-polarization-channel reconstructions of the narrowband beam, presented in Supplement 1, Section 6, confirm that BBSSP is polarization sensitive, but to demonstrate polarization-sensitive spatiospectral characterization, we applied BBSSP to measure a broadband vector pulse-beam. The broadband vector pulse-beam was reconstructed with 17 spectral channels of 5 nm subbandwidth covering a total bandwidth of 760 to 840 nm and two polarization channels for each spectral channel. Rows (a) and (b) of Fig. 5 show the reconstructed spectrally resolved probe fields for each of the two orthogonal polarization states in the pulse-beam. It is worth noting that the technique produces accurate reconstructions even in the presence of zeros in the amplitude. Here, as well as in the vortex beam reconstructions (Fig. 3), the spatial phase is accurately retrieved despite the zero in the spatial amplitude, and Supplement 1, Section 5 demonstrates accurate retrieval of a pulse-beam with a zero in the spectral

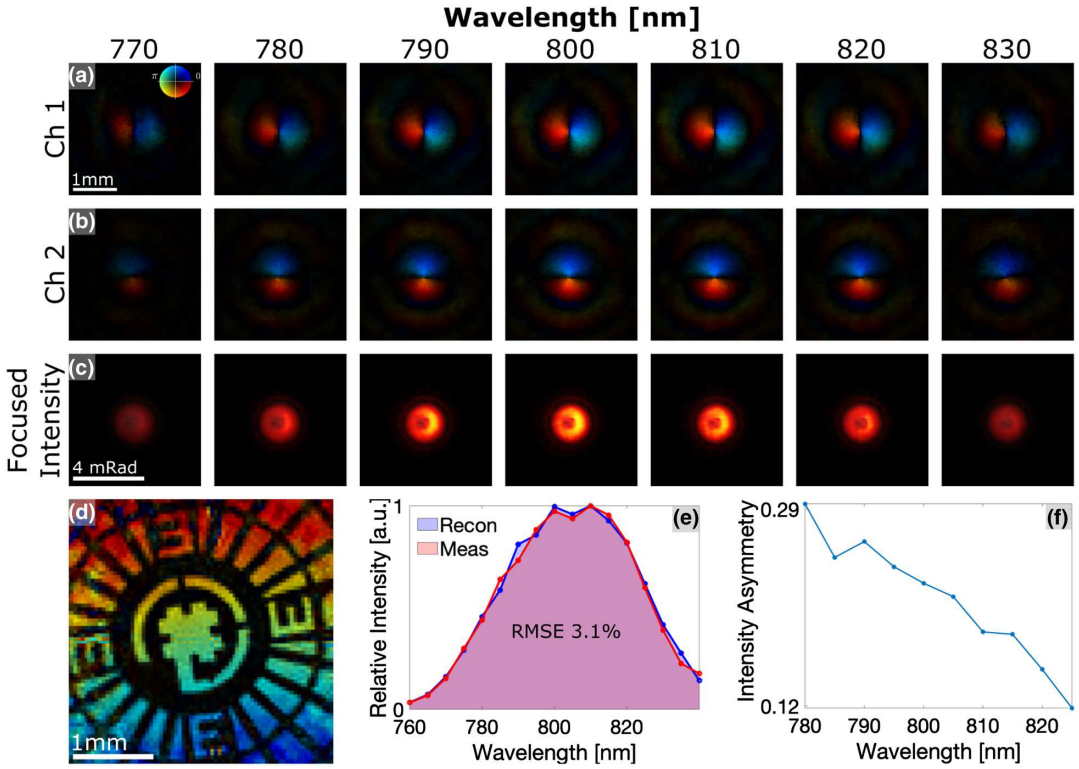

Fig. 5. Polarization-sensitive spatiospectral characterization of a broadband vector pulse-beam. Rows (a) and (b) show selected reconstructed probe channels. All reconstructed probe channels are shown Supplement 1, Fig. S6. (a) The vertically polarized portion of the pulse-beam and (b) the horizontally polarized portion. The scale bar in (a) is common to both rows. Row (c) shows the spectrally resolved intensity of the vector pulse-beam at focus, which is calculated as the summed intensity of the Fourier transform of the corresponding polarization channels. The scale bar in (c) is common to the row. (d) Reconstructed object transmission profile. (e) The measured and reconstructed spatially averaged spectra. The RMSE between the reconstructed and measured spatially averaged spectra is 3.1%. (f) The focused intensity asymmetry as a function of wavelength. The intensity asymmetry (A_I) is calculated as $A_I = \frac{R-L}{R+L}$, where $R(L)$ is the maximum intensity on the right (left) side of the singularity.

amplitude. BBSSP is a nonlocal diffractive technique because different portions of the beam interfere with each other. This mixing allows the technique to retrieve any sign changes in the field and allows us to distinguish from zeros that occur in amplitude without phase change. Other than overall amplitude variation, little spectral dependence can be observed in the reconstructed probe fields. However, if we consider the summed intensity of the Fourier transform of the two polarization channels for each spectral component, as shown in row (c) of Fig. 5, the spectral dependence is clearly visible. Since the pulse-beam was collimated at the object plane, the Fourier transform of the reconstructed field gives the field at focus. The intensities shown in row (c) are what would be seen by a CCD detector placed at the focus of the spectrally filtered pulse-beam. This analysis reveals spectral dependence of the reconstructed pulse-beams, and it highlights one of the benefits of full-field spatiospectral characterization: the results can be used to determine the spatiospectral field at any other axial plane. This enables characterization of high-intensity pulse-beams at focus by making measurements away from focus. We quantified the spectral dependence observed in the spectrally resolved intensities at focus by considering the horizontal asymmetry of the intensity profiles. To do so, we quantified the ratio of the maximum intensity on the left and right side of the singularity for each spectral component as $A_I = \frac{R-L}{R+L}$, where A_I is the intensity asymmetry and $R(L)$ is the maximum intensity on the right (left) side of the singularity. The results of this analysis are displayed in Fig. 5(f), which shows a nearly linear trend of the intensity asymmetry as a function of wavelength. These results qualitatively agree with simulations of the s-wave plate's impact on wavelengths other than the design wavelength of the waveplate [64].

4. CONCLUSION

Spatiospectral structure is ubiquitous in pulse-beams. Generating highest intensity light fields requires mitigating spatiospectral distortions, but spatiospectral structure can also be used to shape light for particular applications (SSTF, STED, micromachining) [11,12,14–18]. Optimal mitigation or application of spatiospectral structure necessitates sophisticated pulse-beam measurement techniques. Here we have demonstrated pulse-beam metrology with broadband single-shot ptychography, which is the first reference-free, full-field, single-shot spatiospectral characterization technique to our knowledge.

We verified that Gaussian, spatially structured, and spatiospectrally structured pulse-beams are accurately reconstructed by BBSSP. We also showed that BBSSP can characterize a single-pulse-beam. Additionally, we demonstrated that BBSSP enables simultaneous demultiplexing of multiple sources of incoherence by reconstructing orthogonal polarization states for each spectral channel of a vector pulse-beam. BBSSP enables simple, high-speed, spatiospectral characterization that has the potential to revolutionize the application and mitigation of spatiospectral structure for pulse-beam control. The current BBSSP system allows for characterization of many ultrafast pulse-beams of interest, and its

capabilities (spatial resolution, field of view, spectral resolution, allowable spectral bandwidth, data collection rate, and reconstruction rate) can be expanded as described in Supplement 1, Section 11, so that BBSSP should be applicable to nearly all pulse-beams. Implementing BBSSP in the x-ray regime is a particularly exciting prospect, as it would provide real time shot-to-shot characterization of self-amplified spontaneous emission and seeded pulses from FELs.

Funding. Air Force Office of Scientific Research (FA9550-20-1-0143); National Science Foundation (2010359); NVIDIA (Academic Hardware Grant Program); H2020 European Research Council (851154 (ULTRAIMAGE)); European Research Council (ENIGMA 789116).

Acknowledgment. We acknowledge Ella Maru Studio for producing the BBSSP system image shown in Fig. 1(a). We acknowledge fruitful conversations with Professor Jeff Squier.

Disclosures. The authors declare no conflicts of interest.

Data availability. Data underlying the results presented in this paper are not publicly available at this time but may be obtained from the authors upon reasonable request.

Supplemental document. See Supplement 1 for supporting content.

REFERENCES

1. A. McPherson, G. Gibson, H. Jara, U. Johann, T. S. Luk, I. A. McIntyre, K. Boyer, and C. K. Rhodes, "Studies of multiphoton production of vacuum-ultraviolet radiation in the rare gases," J. Opt. Soc. Am. B **4**, 595–601 (1987).
2. X. F. Li, A. Lhuillier, M. Ferray, L. A. Lompré, and G. Mainfray, "Multiple-harmonic generation in rare gases at high laser intensity," Phys. Rev. A **39**, 5751–5761 (1989).
3. T. Popmintchev, M. C. Chen, D. Popmintchev, P. Arpin, S. Brown, S. Ališauskas, G. Andriukaitis, T. Balčiunas, O. D. Mücke, A. Pugzlys, A. Baltuška, B. Shim, S. E. Schrauth, A. Gaeta, C. Hernández-García, L. Plaja, A. Becker, A. Jaron-Becker, M. M. Murnane, and H. C. Kapteyn, "Bright coherent ultrahigh harmonics in the keV x-ray regime from mid-infrared femtosecond lasers," Science **336**, 1287–1291 (2012).
4. C. G. Durfee, A. R. Rundquist, S. Backus, C. Herne, M. M. Murnane, and H. C. Kapteyn, "Phase matching of high-order harmonics in hollow waveguides," Phys. Rev. Lett. **83**, 2187–2190 (1999).
5. A. Popp, J. Vieira, J. Osterhoff, Z. Major, R. Hörlein, M. Fuchs, R. Weingartner, T. P. Rowlands-Rees, M. Marti, R. A. Fonseca, S. F. Martins, L. O. Silva, S. M. Hooker, F. Krausz, F. Grüner, and S. Karsch, "All-optical steering of laser-wakefield-accelerated electron beams," Phys. Rev. Lett. **105**, 215001 (2010).
6. D. H. Froula, J. P. Palastro, D. Turnbull, A. Davies, L. Nguyen, A. Howard, D. Ramsey, P. Franke, S. W. Bahk, I. A. Begishev, R. Boni, J. Bromage, S. Bucht, R. K. Follett, D. Haberberger, G. W. Jenkins, J. Katz, T. J. Kessler, J. L. Shaw, and J. Vieira, "Flying focus: spatial and temporal control of intensity for laser-based applications," Phys Plasmas **26**, 032109 (2019).
7. A. M. Wilhelm and C. G. Durfee, "Tilted snowplow ponderomotive electron acceleration with spatio-temporally shaped ultrafast laser pulses," Front. Phys. **7**, 1–11 (2019).
8. A. Braun, X. Liu, G. Korn, D. Du, J. Squier, and G. Mourou, "Self-channeling of intense femtosecond laser pulses in air," Opt. Lett. **20**, 73–75 (1995).
9. J. Li, W. Tan, J. Si, S. Tang, Z. Kang, and X. Hou, "Control of the spatial characteristics of femtosecond laser filamentation in glass via feedback-based wavefront shaping with an annular phase mask," Opt. Express **29**, 5972–5981 (2021).
10. M. Scheller, M. S. Mills, M. A. Miri, W. Cheng, J. V. Moloney, M. Kolesik, P. Polynkin, and D. N. Christodoulides, "Externally refuelled optical filaments," Nat. Photonics **8**, 297–301 (2014).
11. A. Elgohary, E. Block, J. Squier, M. Koneshloo, R. K. Shaha, C. Frick, J. Oakey, and S. A. Aryana, "Fabrication of sealed sapphire microfluidic devices using femtosecond laser micromachining," Appl. Opt. **59**, 9285–9291 (2020).
12. J. Cheng, C. S. Liu, S. Shang, D. Liu, W. Perrie, G. Dearden, and K. Watkins, "A review of ultrafast laser materials micromachining," Opt. Laser Technol. **46**, 88–102 (2013).
13. J. Schwinger, "On gauge invariance and vacuum polarization," Phys. Rev. **82**, 664–679 (1951).
14. G. Zhu, J. Howe, M. Durst, W. Zipfel, and C. Xu, "Simultaneous spatial and temporal focusing of femtosecond pulses," Opt. Express **13**, 2153–2159 (2005).
15. E. Block, M. Greco, D. Vitek, O. Masihzadeh, D. A. Ammar, M. Y. Kahook, N. Mandava, C. Durfee, and J. Squier, "Simultaneous spatial and temporal focusing for tissue ablation," Biomed. Opt. Express **4**, 831–841 (2013).
16. N. Jhajj, I. Larkin, E. W. Rosenthal, S. Zahedpour, J. K. Wahlstrand, and H. M. Milchberg, "Spatiotemporal optical vortices," Phys. Rev. X **6**, 031037 (2016).
17. S. W. Hell and J. Wichmann, "Breaking the diffraction resolution limit by stimulated emission: stimulated-emission-depletion fluorescence microscopy," Opt. Lett. **19**, 780–782 (1994).
18. D. Wildanger, E. Rittweger, L. Kastrup, and S. W. Hell, "STED microscopy with a supercontinuum laser source," Opt. Express **16**, 9614–9621 (2008).
19. R. A. Fisher and J. A. Fleck, "On the phase characteristics and compression of picosecond pulses," Appl. Phys. Lett. **15**, 287–290 (1969).
20. R. Trebino, "The most important paper you've never read," Opt. Photon. News **31**(1), 46–53 (2020).
21. R. Trebino and D. J. Kane, "Using phase retrieval to measure the intensity and phase of ultrashort pulses: frequency-resolved optical gating," J. Opt. Soc. Am. A **10**, 1101–1111 (1993).
22. D. J. Kane and R. Trebino, "Single-shot measurement of the intensity and phase of an arbitrary ultrashort pulse by using frequency-resolved optical gating," Opt. Lett. **18**, 823–825 (1993).
23. P. O'Shea, M. Kimmel, X. Gu, and R. Trebino, "Highly simplified device for ultrashort-pulse measurement," Opt. Lett. **26**, 932–934 (2001).
24. B. C. Platt and R. Shack, "History and principles of Shack-Hartmann wavefront sensing," J. Refract. Surg. **17**, S573–S577 (2001).
25. C. Dorrer, "Spatiotemporal metrology of broadband optical pulses," IEEE J. Sel. Top. Quantum Electron. **25**, 3100216 (2019).
26. Y. Liu, J. E. Beetar, J. Nesper, S. Gholam-Mirzaei, and M. Chini, "Single-shot measurement of few-cycle optical waveforms on a chip," Nat. Photonics **16**, 109–112 (2021).
27. S. W. Jolly, O. Gobert, and F. Quéré, "Spatio-temporal characterization of ultrashort laser beams: a tutorial," J. Opt. **22**, 103501 (2020).
28. D. E. Adams, T. A. Planchon, A. Hrin, J. A. Squier, and C. G. Durfee, "Characterization of coupled nonlinear spatiospectral phase following an ultrafast self-focusing interaction," Opt. Lett. **34**, 1294–1296 (2009).
29. S. Akturk, X. Gu, P. Bowlan, and R. Trebino, "Spatio-temporal couplings in ultrashort laser pulses," J. Opt. **12**, 093001 (2010).
30. A. Borot and F. Quéré, "Spatio-spectral metrology at focus of ultrashort lasers: a phase-retrieval approach," Opt. Express **26**, 26444–26461 (2018).
31. G. Pariente, V. Gallet, A. Borot, O. Gobert, and F. Quéré, "Space-time characterization of ultra-intense femtosecond laser beams," Nat. Photonics **10**, 547–553 (2016).
32. A. Jeandet, A. Borot, K. Nakamura, S. W. Jolly, A. J. Gonsalves, C. Tóth, H.-S. Mao, W. P. Leemans, and F. Quéré, "Spatio-temporal structure of a petawatt femtosecond laser beam," J. Phys. **1**, 035001 (2019).
33. S. L. Cousin, J. M. Bueno, N. Forget, D. R. Austin, and J. Biegert, "Three-dimensional spatiotemporal pulse characterization with an acousto-optic pulse shaper and a Hartmann–Shack wavefront sensor," Opt. Lett. **37**, 3291–3293 (2012).
34. E. Rubino, D. Faccio, L. Tartara, P. K. Bates, O. Chalus, M. Clerici, F. Bonaretti, J. Biegert, and P. Di Trapani, "Spatiotemporal amplitude and phase retrieval of space-time coupled ultrashort pulses using the Shackled-FROG technique," Opt. Lett. **34**, 3854–3856 (2009).
35. B. Alonso, Í. J. Sola, Ó. Varela, J. Hernández-Toro, C. Méndez, J. San Román, A. Zaïr, and L. Roso, "Spatiotemporal amplitude-and-phase reconstruction by Fourier-transform of interference spectra of high-complex-beams," J. Opt. Soc. Am. B **27**, 933–940 (2010).
36. P. Gabolde and R. Trebino, "Single-shot measurement of the full spatio-temporal field of ultrashort pulses with multi-spectral digital holography," Opt. Express **14**, 11460–11467 (2006).

37. P. Bowlan, P. Gabolde, A. Shreenath, K. McGresham, R. Trebino, and S. Akturk, "Crossed-beam spectral interferometry: a simple, high-spectral-resolution method for completely characterizing complex ultrashort pulses in real time," Opt. Express **14**, 11892–11900 (2006).
38. M. Jean-Baptiste, C. Zhao, L.-M. Rodrigo, and O. Thomas, "Single-shot diagnosing of spatiotemporal couplings in ultrashort laser pulses by spatiospectral imaging of a third-order nonlinear process," Opt. Lett. **45**, 2207–2210 (2020).
39. L. Chopineau, A. Denoeud, A. Leblanc, E. Porat, P. Martin, H. Vincenti, and F. Quéré, "Spatio-temporal characterization of attosecond pulses from plasma mirrors," Nat. Phys. **17**, 968–973 (2021).
40. D. Goldberger, D. Schmidt, J. Barolak, B. Ivanic, C. G. Durfee, and D. E. Adams, "Spatiospectral characterization of ultrafast pulse-beams by multiplexed broadband ptychography," Opt. Express **29**, 32474–32490 (2021).
41. R. Hegerl and W. Hoppe, "Dynamische Theorie der Kristallstrukturanalyse durch Elektronenbeugung im inhomogenen Primärstrahlwellenfeld," Ber. Bunsenges. Phys. Chem. **74**, 1148–1154 (1970).
42. J. M. Rodenburg and H. M. L. Faulkner, "A phase retrieval algorithm for shifting illumination," Appl. Phys. Lett. **85**, 4795–4797 (2004).
43. J. M. Rodenburg, A. C. Hurst, A. G. Cullis, B. R. Dobson, F. Pfeiffer, O. Bunk, C. David, K. Jefimovs, and I. Johnson, "Hard-x-ray lensless imaging of extended objects," Phys. Rev. Lett. **98**, 034801 (2007).
44. J. M. Rodenburg, "Ptychography and related diffractive imaging methods," in *Advances in Imaging and Electron Physics* (2008).
45. A. M. Maiden and J. M. Rodenburg, "An improved ptychographical phase retrieval algorithm for diffractive imaging," Ultramicroscopy **109**, 1256–1262 (2009).
46. P. Thibault, M. Dierolf, O. Bunk, A. Menzel, and F. Pfeiffer, "Probe retrieval in ptychographic coherent diffractive imaging," Ultramicroscopy **109**, 338–343 (2009).
47. A. Rana, J. Zhang, M. Pham, A. Yuan, Y. H. Lo, H. Jiang, S. Osher, and J. Miao, "Potential of attosecond coherent diffractive imaging," Phys. Rev. Lett. **125**, 086101 (2019).
48. P. Thibault and A. Menzel, "Reconstructing state mixtures from diffraction measurements," Nature **494**, 68–71 (2013).
49. D. J. Batey, D. Claus, and J. M. Rodenburg, "Information multiplexing in ptychography," Ultramicroscopy **138**, 13–21 (2014).
50. B. K. Chen, P. Sidorenko, O. Lahav, O. Peleg, and O. Cohen, "Multiplexed single-shot ptychography," Opt. Lett. **43**, 5379–5382 (2018).
51. B. Enders, "Development and application of decoherence models in ptychographic diffraction imaging," Doctoral dissertation (Technische Universität München, 2016).
52. R. Karl, C. Bevis, R. Lopez-Rios, J. Reichanadter, D. Gardner, C. Porter, E. Shanblatt, M. Tanksalvala, G. F. Mancini, M. Murnane, H. Kapteyn, and D. Adams, "Spatial, spectral, and polarization multiplexed ptychography," Opt. Express **23**, 30250–30258 (2015).
53. P. Sidorenko, O. Lahav, and O. Cohen, "Ptychographic ultrahigh-speed imaging," Opt. Express **25**, 10997–11008 (2017).
54. O. Wengrowicz, O. Peleg, B. Loevsky, B. K. Chen, G. I. Haham, U. S. Sainadh, and O. Cohen, "Experimental time-resolved imaging by multiplexed ptychography," Opt. Express **27**, 24568–24577 (2019).
55. J. Barolak, D. Goldberger, J. Squier, Y. Bellouard, C. Durfee, and D. Adams, "Wavelength-multiplexed single-shot ptychography," Ultramicroscopy **233**, 113418 (2021).
56. D. Schmidt, D. Goldberger, A. D. L. Heras, C. Hernández-García, Y. Lei, P. Kazansky, D. Adams, and C. Durfee, "Characterization of highly structured high harmonic beams through multiplexed broadband ptychography," in *Frontiers in Optics + Laser Science* (Optical Society of America, 2021), paper FM5D.3.
57. P. Sidorenko and O. Cohen, "Single-shot ptychography," Optica **3**, 9–14 (2016).
58. X. Pan, C. Liu, and J. Zhu, "Single shot ptychographical iterative engine based on multi-beam illumination," Appl. Phys. Lett. **103**, 171105 (2013).
59. D. F. Gardner, M. Tanksalvala, E. R. Shanblatt, X. Zhang, B. R. Galloway, C. L. Porter, R. Karl, Jr., C. Bevis, D. E. Adams, H. C. Kapteyn, M. M. Murnane, and G. F. Mancini, "Subwavelength coherent imaging of periodic samples using a 13.5 nm tabletop high-harmonic light source," Nat. Photonics **11**, 259–263 (2017).
60. D. G. Hall, "Vector-beam solutions of Maxwell's wave equation," Opt. Lett. **21**, 9–11 (1996).
61. L. Ye, J. R. Rouxel, S. Asban, B. Rösner, and S. Mukamel, "Probing molecular chirality by orbital-angular-momentum-carrying x-ray pulses," J. Chem. Theory Comput. **15**, 4180–4186 (2019).
62. J. Ni, S. Liu, G. Hu, Y. Hu, Z. Lao, J. Li, Q. Zhang, D. Wu, S. Dong, J. Chu, and C.-W. Qiu, "Giant Helical dichroism of single chiral nanostructures with photonic orbital angular momentum," ACS Nano **15**, 2893–2900 (2021).
63. M. V. Berry, "Optical vortices evolving from helicoidal integer and fractional phase steps," J. Opt. A **6**, 259–268 (2004).
64. M. Gecevivius, "Polarization sensitive optical elements by ultrafast laser nanostructuring of glass," Ph.D. thesis (University of Southampton, 2014).